# Characterizing and Correcting Hyperion Detectors using Ice-Sheet Images

Robert Bindschadler (Oceans and Ice Branch, Laboratory for Hydrospheric Processes, NASA Goddard Space Flight Center, Greenbelt, MD 20771; 301-614-5707; bob@igloo.gsfc.nasa.gov)

Hyeungu Choi (SAIC, Beltsville, MD 20705-2675)

## *Abstract*

Two Hyperion images of the Greenland ice sheet are used to characterize errors in the VNIR and SWIR detector arrays of Hyperion. Spatial variability in detector output is seen in both arrays and, in both cases, is largest at the shorter wavelengths and decreases as wavelength increases. Standard deviations of the maximum variability are 40 DN for the VNIR array and 123 DN for the SWIR array. Temporal stability is nearly as large and exhibits the same spectral characteristics of large variability at shorter wavelengths and decreasing with increasing wavelengths. The uniformity and stability of the ice-sheet surface enables a detailed characterization and emphasizes the utility of using ice sheets as targets to achieve on-orbit sensor characterization.

## *Introduction*

Hyperion is the first satellite-based hyperspectral sensor. Launched in November, 2000, on the Earth-Observing-1 (EO-1) platform, it is part of NASA's New Millennium Program whose goal is to develop and demonstrate new technologies for space-based research. In the case of the EO-1 program, a Science Validation Team was established to investigate the utility of Hyperion and two other instruments (Advanced Land Imager and Leisa Atmospheric Corrector) for earth science studies. One of us (RB) was a team member and led a set of coinvestigators whose assessments included a wide range of applications on snow and ice (Bindschadler, this volume; Scambos and others, this volume). Many images of ice sheets were collected to support these studies. The nearly homogeneous character of the ice-sheet surface also provides an opportunity to characterize the imaging instruments with a natural "flat-field" target. This paper reports on this characterization of the Hyperion detectors, including the stability of the detectors, and illustrates a means to correct for the detector variations found.

## *Hyperion*

Hyperion is a push-broom type sensor that measures the incoming radiation at the instrument across 220 spectral bands in the 400-2500 nm wavelength range with a spectral resolution of 10 nm (http://eo1.gsfc.nasa.gov). Images are collected of the earth with a spatial resolution of 30 meters across a swath 7.5 km wide. This is accomplished by recording the spatial and spectral information on two multi-detector arrays. A charged-couple device (CCD) spectrometer produces the first 70 channels in the visible

and near infrared (VNIR) wavelengths (400-1000 nm) while a HgCdTe spectrometer produces channels 71 through 242 in the shortwave infrared (SWIR) wavelengths (900-2500 nm). Both spectrometers share the same fore-optics.

The spectrum for each 30-m pixel across the swath is measured by a separate set of detectors. Ideally, the detectors for every pixel respond identically in their analog-to-digital characteristics, but this is never achieved, in practice. Pre-launch calibration of this array determined corrections to account for detector variability. These corrections were applied during Level 1 processing of Hyperion data performed at TRW, the Hyperion instrument manufacturer.

## *Ice-Sheet Data*

Hyperion data of ice sheets were collected for purposes ranging from albedo determination to cloud/snow discrimination (Ref papers in this volume). Here we use images of extremely homogenous regions of the ice sheet to minimize target-related variations in Hyperion data. The large extent of these homogenous areas further promotes their use as a "flat-field" target when image data are averaged over many lines. By this approach, we can attribute spatial variations to detector variability of the Hyperion instrument.

The two Hyperion images used in this paper were collected of the "Crawford Point" site in western Greenland (69.88$^{o}$N, 46.98$^{o}$W) on July 7 (day 188), 2001 and 32 days later on August 8 (day 220), 2001. At this site, the surface is composed exclusively of very gently undulated topography with a mean surface slope of approximately 0.5$^{o}$ and surface reflectivity variations of less than 1%. The uniform character of this surface extended across the entire swath (256 pixels). Along the groundtrack, this surface persisted for 3500 lines (105 km) in the day 188 image, but in the day 220 image was limited by clouds to 236 lines (7.08 km).

The measured spectral radiances of these image subsets are shown in Figure 1. The day 188 image is brighter, probably due to a higher sun elevation (closer to the summer solstice) and possible atmospheric differences. Atmospheric differences on the two dates also might contribute to the pixel-to-pixel differences, but the high degree of correlation in the inferred sensor characteristics shown later suggests this effect is less significant.

The uniform nature of the target enhances the ability to see stripes in both images parallel to the satellite ground track. Figure 1 shows the standard deviation of the measured radiances (in DN units). The magnitude of the standard deviations is largest in the near infrared where it reaches 1000 DN and may indicate the presence of atmospheric water vapor. At longer wavelengths, the radiances range over a few hundred DNs and in the visible portion of the spectrum, they range over a few tens of DNs. Histograms of the radiances in the more reflective bands for snow had a half width of approximately 100 digital numbers (DN) (116 DN for the most reflective band 13 at 478.4 nm). We show later that the magnitude of uncorrected detector outputs can be as large as a few tens of DNs, a magnitude comparable to range of the measured radiances. This is why the

stripes are so easily seen in images of uniform targets, such as the ice sheet images considered here.

## *Data Processing and Detector Characterization*

No atmospheric correction was applied to either image. The 242 spectral channels were reduced to 147 by omitting the water vapor absorption channels (bands 121 to 130 and 167 to 181), a set of redundant channels in the overlap area (bands 57 to 77 covering 900-1000 nm) and two bands (143 and 190, at 1578 and 2052, respectively) with negative mean radiances.

Additional processing was required to identify "unreliable" detectors and adjust the data produced by them. These isolated detectors were identified by examining each band separately. Across each line (a line is composed of the 256 pixels across the image swath), a detector was labeled as "suspect" if its DN value was more than four standard deviations away from the mean DN value of that line. If the same detector was suspect for more than 50% of the lines in the image, it was labeled as unreliable and the DN values of those pixels were replaced by a value equal to the average of its two neighbors on the same line. For the more than 60,000 detectors in the two Hyperion detector arrays (256 pixels by 220 bands), only six unreliable detectors were found in both images. These were located at band/pixel pairs 56/147, 94/82, 99/81, 116/127, 119/240, 120/240. In addition detector 165/148 was judged unreliable and corrected in the day 188 image suggesting some temporal variability to detector performance (Han and others, 2002).

Following this processing, the 256-pixel wide lines of each image were averaged for each band over 3500 lines (for day 188) or 236 lines (for day 220) of the image. Figure 2 shows typical profiles (band 120 centered at 1346 nm). For illustration of the data departures caused by unreliable detectors, Figure 2 includes the data at pixel number 240 prior to the correction method described above.

Image stripes parallel to the satellite motion, i.e., orthogonal to the image swath, are represented in averaged line profiles by sudden deviations in average DN at the pixel scale. One such example is in the region of pixel #160 in Figure 2.

To examine the pixel-to-pixel differences for different spectral bands, the averaged line profile for each band and date was differenced from a smoothed cubic spline fit to the data for that band and date. The precise shape of the spline depended on a tension parameter (Gao. 1998). A tension value of 40 was chosen, but the shape of the curve was stable whenever the tension value exceeded 10. Figure 3 plots the "data minus spline" differences for each pixel and for each band as an image. Because we claim these images are of a near-uniform-reflectance target, Figure 3 is the estimated error of the VNIR and SWIR detector arrays for each day. Correlation coefficients of the 256 pixel errors for each spectral band for the two dates were calculated. The mean correlation coefficient was 0.6 with a standard deviation of 0.1.

There is a similar strong spectral signature evident in both panels of Figure 3 and a high pixel-scale variability. This is represented in Figure 4 by showing the standard deviation

of the 256-pixel distribution of errors (shown in Figure 3) for each spectral band. The mean error at each spectral band was very nearly zero, as expected from the cubic-spine smoothing used. Figure 4 presents the results for day 188, but the results are nearly identical for day 220. The largest VNIR variability of nearly 40 DN occurs at the shortest wavelength, but it rapidly drops to less than 10 DN over the rest of the array. The SWIR variability also is largest, at 123 DN, for the shortest SWIR wavelength and it, too, decreases as wavelength increases, but the decrease is more gradual than in the VNIR array. At wavelengths longer than 1400 nm, the measured reflectance of the ice sheet is very small, possibly limiting our ability to characterize detector errors in this part of the spectrum.

While the magnitude of the variability of detector errors (Figure 4) for day 188 are very similar to those for day 220 and the general appearance of the pattern of the error arrays for each day are also similar, the specific error values are quite different. The difference between the two error arrays was calculated and in Figure 4, the standard deviations of this error array difference are plotted for each spectral band. They are almost as large in magnitude as the variability of the error itself. This indicates the Hyperion detector arrays have a temporally stable level of variability, yet the pattern of variability is temporally unstable.

Details of the date-independent band-to-band variability were examined by calculating the cross-correlation between each band pair. Figure 5 shows that the results for the two days give a consistent pattern, some of which was apparent from the discussion of Figure 4 and some of which is new. The diagonals in Figure 5 are the non-lagged autocorrelation value of 1. There are square areas defined by boundaries where the detector characteristics change suddenly. The boundary at 950 nm falls between the VNIR and SWIR detector arrays. This boundary has a ready explanation from Figure 4, but there is also a very prominent boundary at 650 nm and suggestions of less prominent boundaries. Some of these, like the 650 nm example, are present on both dates and some are not. There is also a very curious correlation in the VNIR detectors indicated by an inversely sloped (i.e., upper right to lower left) bright line in Figure 5. It indicates a high correlation of bands centered on bands 35 and 36 (at 712.3 nm) but with an increasing lag across the entire VNIR array. These central bands also define the boundary of the most prominent cross-correlation square within the VNIR array.

Many of our results rest on the assumption that the ice-sheet provides a nearly uniform target and that the line averaging provides a further “flattening” of this target. To check this assumption, the 3500-line day 188 image was divided into two halves of 1750 lines each. Each sub-image was treated as an independent image and treated in a manner similar to the images from days 188 and 220. The correlation of the two new detector error arrays (Figure 3) was 0.95. This gives strong support to the claim that the target, averaged over many lines, is virtually without any spatial variability.

## *Detector Correction Methods*

Given the temporal variability in the detector errors, any set of corrections is short lived. Nevertheless, with the errors already calculated for these two images, we explore two

simple means of correcting the radiances. The first method subtracts the error, so the averaged line profile matches the smoothed cubic spline profile. This is qualitatively very successful in the image area studied, but even just outside this area, some stripes begin to be evident. The second method is to use the ratio of the measured averaged line profile to the smoothed cubic spline. This accounts better for image areas where the spectral radiance is much different than in the study area, but leads to very large, and often implausible, corrections for spectral bands where the ratio is based on a low radiance.

As one visible example of applying the corrections directly to the area outside the study area, we show Figure 6. The image includes a small dark lake to illustrate the success of the correction method to regions of a much lower radiance. The stripes in this subimage are significantly reduced, though not removed entirely. As further evidence of the suppression of striping, Figure 6 also shows the $4^{th}$ and $11^{th}$ MNF bands of both the uncorrected and corrected images.

## *Conclusions*

Ice sheet imagery provides an excellent target for characterizing the internal variability and temporal stability of the two Hyperion detector arrays. The image data appear to be extremely uniform when averaged over even short distances of a few hundred pixels. The spectral signatures also appear stable in time, with differences due to sun elevation.

Our analysis shows that variability of the Hyperion detector arrays occurs across the swath direction, in the spectral dimension and also in the temporal dimension. At a given spectral position, the variability of the detector error across the swath is roughly of the same magnitude as the temporal stability of the detectors. This variability is greatest at the shorter wavelengths of both the VNIR and SWIR detector arrays. This variability causing stripes in the imagery, but the effect can be almost completely removed if suitable corrections to the specific scene are recoverable from the imagery. Line-averaging is a useful means to determine suitable corrections, but due to the temporal variability of the detectors, these corrections must be determined either from each image being corrected or from an image taken very soon before or after the scene to be corrected.

The temporal characterization is limited by the use of only two scenes in this analysis. More ice-sheet scenes would strengthen the temporal characterization. Spectrally different targets, especially ones that are dark in the VNIR and bright at wavelengths longer than 1100 nm, if available, also would be useful.

## *References*

Bindschadler, R., this volume. Tracking Sub-Pixel-Scale Sastrugi with Advanced Land Imager.

Gao, Bo-Cai, Ming Liu, and Curtiss O. Davis, A new and fast method for smoothing spectral imaging data, in Airborne Geoscience Workshop Proceedings, 1998

Han, T., D. Goodenough and J. Love, 2002. Detection and correction of abnormal pixels in Hyperion images, IEEE International Geoscience and Remote Sensing Symposium, Toronto, Canada.

Scambos, T.A. and B. Raup, this volume.

## *Figures*

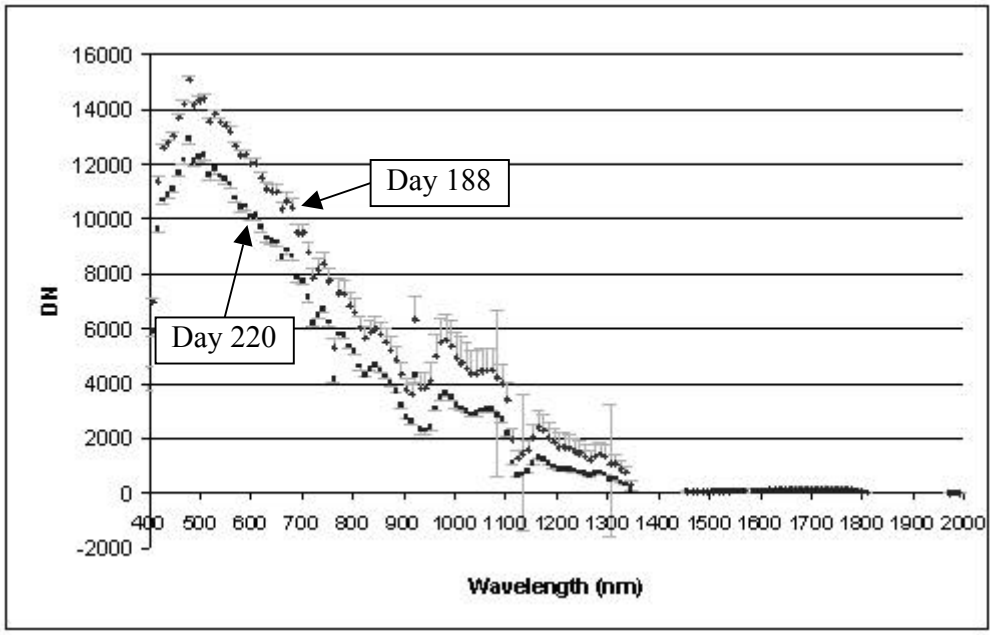


Figure 1. Measured spectral radiances (in units of DN) for the uniform images subsets analyzed in this paper. Points indicate the mean values for each image and bar indicates half the magnitude of the standard deviation.

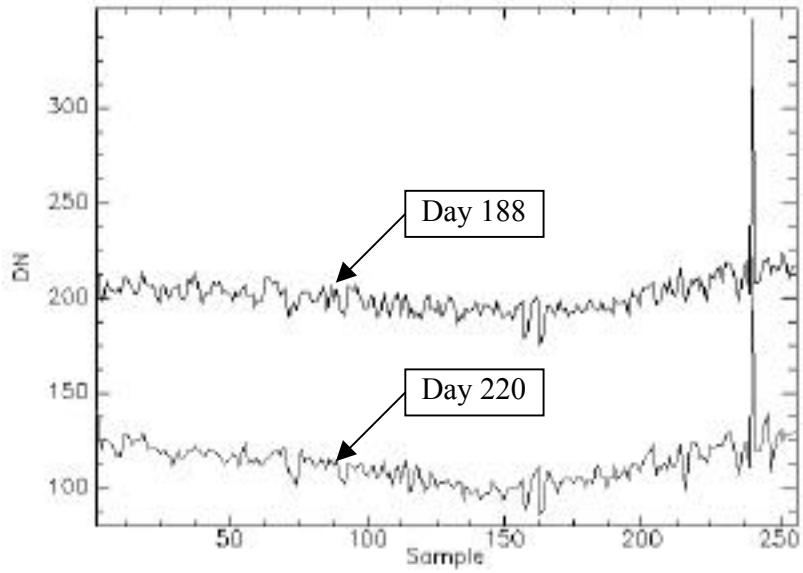


Figure 2. Averaged line profiles of both images for band 120 (1346 nm). Anomaly at pixel 240 illustrates presence of an unreliable detector. Data at this pixel location were corrected as discussed in text.

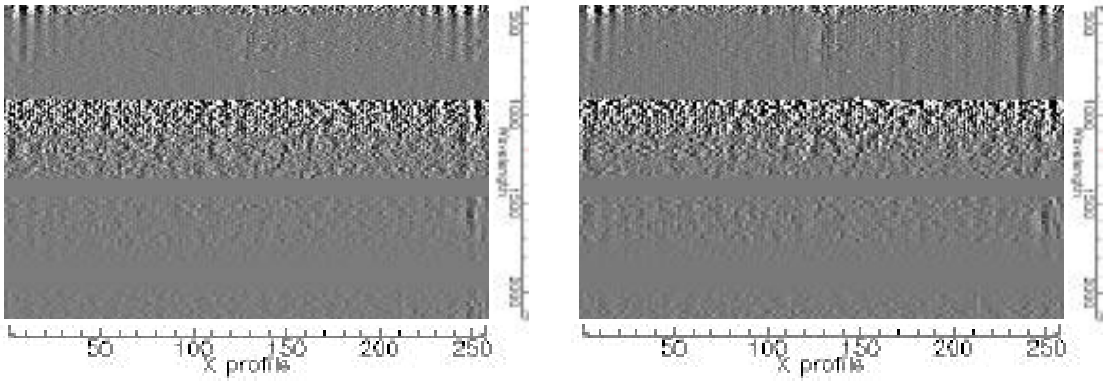


Figure 3. Difference between line-averaged radiance value and cubic-spline smoothed value (in units of DN) for day 188 (left) and day 220 (right). Each panel shows the difference as a gray intensity (dark is a large negative difference; white is a large positive difference) as a function of pixel (horizontal axis) and wavelength (vertical axis).

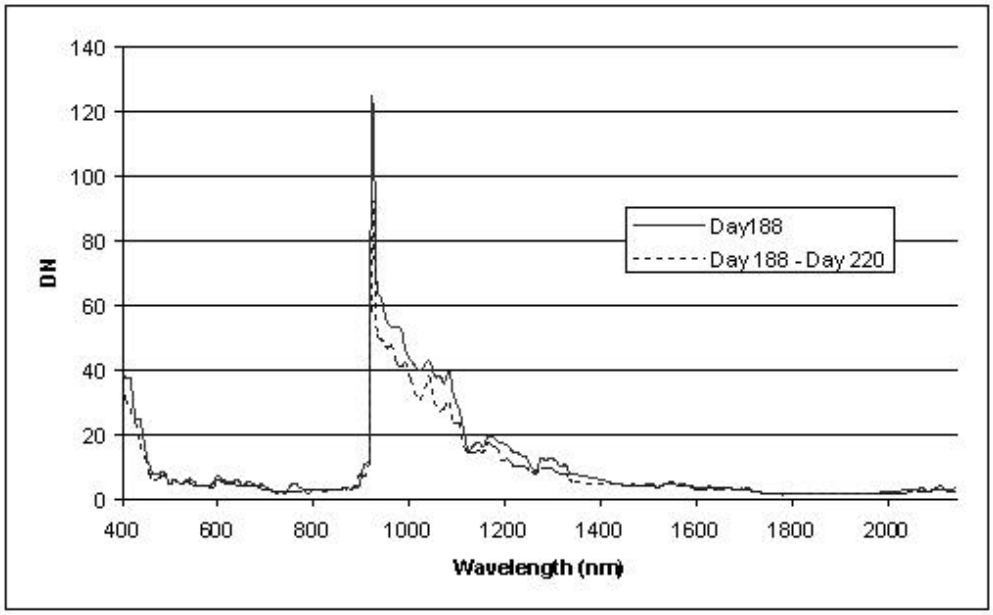


Figure 4. Standard deviations of detector errors (from Figure 3, left panel) for each spectral band and standard deviations of the difference in errors from day 188 and from day 220 for each spectral band.

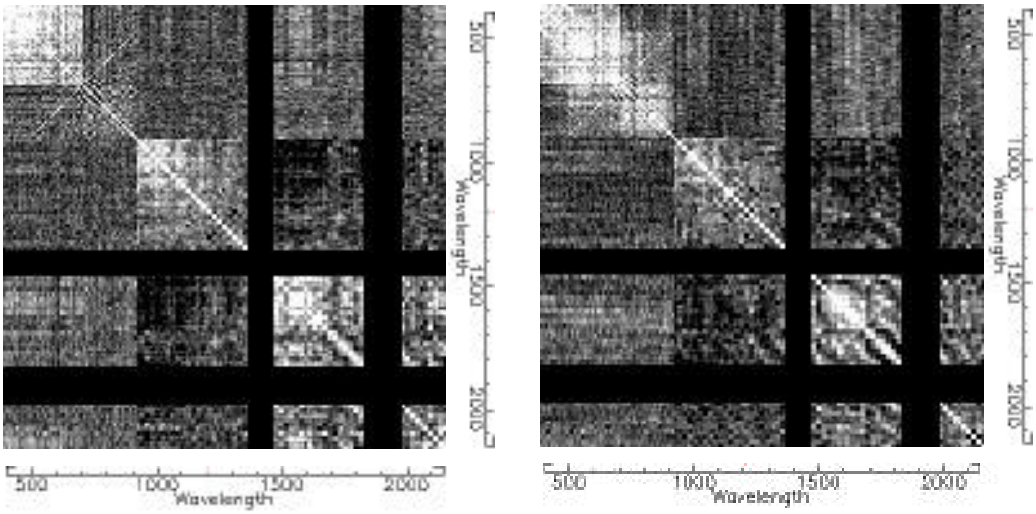


Figure 5. Coefficients of cross-correlation between detector corrections (Figure 3) for all pairs of spectral bands for day 188 (left) and day 220 (right). High positive correlation is bright, high negative correlation is dark. Each image is diagonally symmetric with respect to the upper left to lower right diagonal where correlation coefficient is exactly unity. Black areas correspond to bands omitted from the measured spectra due to the complicating effects of water vapor.

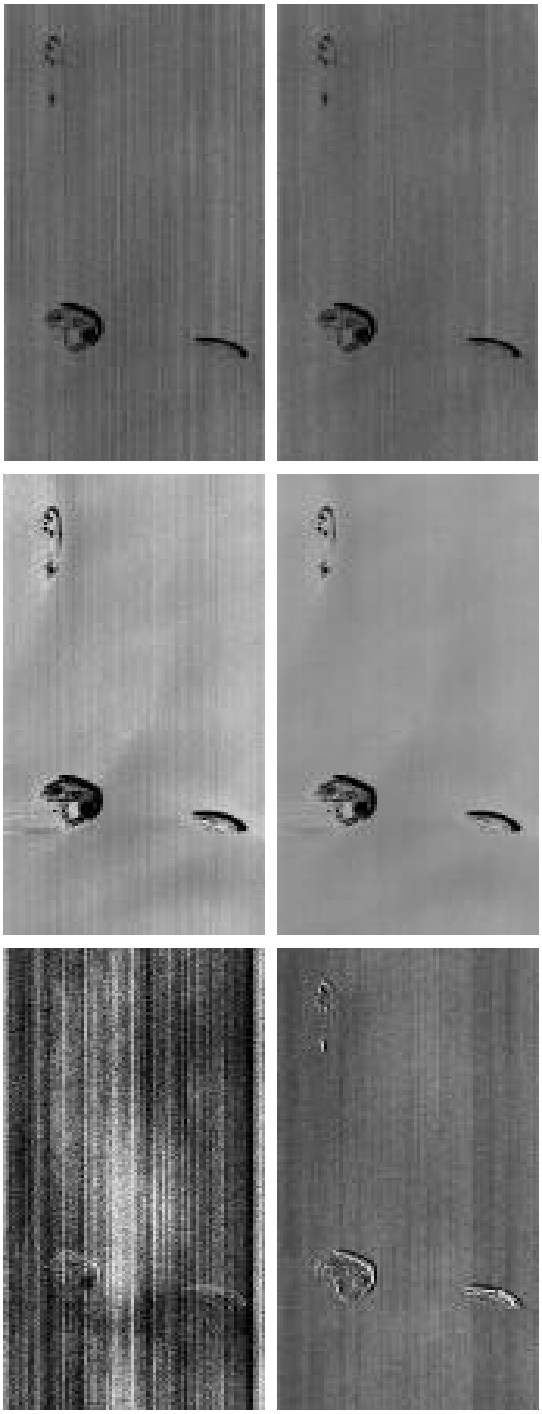

Figure 6. Correction of a short (526-line) portion of Hyperion data of the ice sheet near to the region used in the determination of detector errors. Band 80 (942.8 nm) is shown. Upper pair is the uncorrected (left) and corrected image (right); middle pair is MNF band 4; lower pair is MNF band 11.